Rational Design of Stable Four-Electron-Accepting Carbonyl-*N*-methylpyridinium Species for High-Performance Lithium-Ion Batteries

Xiujuan Wang,[§,1] Wenhao Xue, [§,1] Guangyuan, Gao,[1] Ling Chen,[1] Thomas Baumgartner,[2] Xiaoming He[*,1]*

[*]To whom correspondence should be addressed

[§]These authors contributed equally to this work

[1] Key Laboratory of Applied Surface and Colloid Chemistry (Ministry of Education), School of Chemistry and Chemical Engineering, Shaanxi Normal University, Xi'an 710119, P.R. China

[2] Department of Chemistry, York University, 4700 Keele Street, Toronto, Ontario M3J 1P3, Canada

*Corresponding Author Email: xmhe@snnu.edu.cn

Abstract

Development of novel organics that exhibit multiple and stable redox states, limited solubility and improved conductivity is a highly rewarding direction for improving the performance of lithium-ion batteries (LIBs). As biologically derived organic molecules, carbonylpyridinium compounds have desirable and tunable redox properties, making them suitable candidates for battery applications. In this work, we report a structural evolution of carbonylpyridinium-based redox-active organics, from 2-electron accepting **BMP** to 4-electron accepting small, conjugated molecules (**1**, **2**), and then to the corresponding conjugated polymers (**CP1**, **CP2**). Through suppression of dissolution and increasing electrochemical conductivity, the LIBs performance can be gradually enhanced. At a relatively high current of 0.5 A g^{-1}, high specific capacities for **1** (100 mAh g^{-1}), **2** (260 mAh g^{-1}), **CP1** (360 mAh g^{-1}) and **CP2** (540 mAh g^{-1}) can be reached after 240 cycles. Particularly, the rate performance and cycling stability of **CP2** surpasses many reported commercial inorganic and organic electrode materials. This work provides a promising new carbonylpyridinium-based building block featured with multiple redox centers, on the way to high performance Li-organic batteries.

INTRODUCATION

The application of lithium-ion batteries (LIBs) for energy storage has attracted considerable interest due to their wide use in portable electronics and promising application in high-power electric vehicles.[1, 2] Nowadays, many studies focus on inorganic materials and their carbon-involved composites. But their fabrication consumes a huge amount of energy and releases a large amount of CO_2, which undermines their environmental sustainability. Moreover, the ultimately limited availability of lithium on earth has forced researchers to evaluate alternative electroactive materials for batteries. Compared to inorganic materials, organic compounds are attractive alternative electrode candidates for next-generation LIBs because of their distinct advantages such as lightweight, abundance, non-toxicity, sustainability, flexibility, and simple structure optimization.[3-7] Therefore, replacing inorganic electrodes with organic materials in rechargeable batteries is ideal to alleviate the environmental and sustainability challenges.

Over the past several decades, remarkable progress has been achieved with electroactive organic compounds for LIBs.[7] A number of diverse structural motifs, such as organic free-radicals,[8-11] conjugated carbonyls,[12-19] imine compounds,[20, 21] phenothiazine,[22-25] phenoxazine,[26] benzothiadiazole,[27] dibenzothiophenesulfone,[28] and azobenzenes[29, 30] have been explored as electrodes for batteries. So far however, most of these organic materials are still not competitive enough with high-performing inorganic electrode materials. Their practical application is severely hampered by their high solubility in organic electrolytes and low electronic conductivity, which leads to poor cycling stability and rate performance. Moreover, the charge capacity is generally limited to either one or two electrons per molecule or unit, which limits the overall capacity and energy density of the battery. These constraints have motivated rapidly accelerating fundamental research to identify novel organic molecule that exhibit multiple and stable redox reactions, limited solubility and improved conductivity.

Pyridinium salts demonstrate chemically reversible electrochemical behavior upon reduction. One representative example is the viologen family (quaternized 4,4'-bipyridiniums) that has been widely utilized in electrochromic devices and energy storage, due to their desirable redox properties.[31-37] Another notable example includes the NAD^+/NADH couple that functions as an electron-transfer catalyst in the respiratory chain. The key active motif is the carbonylpyridinium unit, capable of accepting two electrons per unit.[38, 39] By virtue of its two reversible redox events, high theoretical capacity, and its unique structural feature mentioned above, the use of benzoyl-N-methylpyridinium

(**BMP**) derivatives has been proven to be very promising for redox-flow batteries by Sanford and coworkers.[40, 41] However, the exploration of this appealing bio-derived redox-active structure for application in LIBs is considerably underdeveloped, largely due to its high solubility in commonly employed electrolytes.

Several strategies have been devised to address the dissolution problem of small molecule-based materials, such as polymerization or salification. Conjugated polymers, as opposed to their aliphatic counterparts, have particularly great advantage in achieving highly desirable electrical conductivity. The traditional design involves the integration of redox-active moieties in the main chain by conjugation with aromatic linkers. On the other hand, such design has inevitable drawbacks for providing stable redox potentials, due to large charge repulsion from the generated delocalized polarons and bipolarons in the backbone, therefore leading to a low battery performance. Very recently, we reported a rationally designed conjugated polymer with pendant benzoylpyridinium (**BMP**) redox-active units that simultaneously reduce the solubility of the materials and mitigate the charge repulsion to enhance the overall battery performance.[42] The carbonyl linker could effectively minimize the overlap of the HOMO and LUMO orbitals in the materials, allowing the redox centers to operate in a relatively interference-free manner.

Herein, we now report a new rational molecular design strategy and comprehensive study on the performance of next-generation carbonylpyridinium-based redox active materials (Scheme 1). As part of this investigation, we developed the two di-cationic carbonylpyridinium-derivatives **1** and **2** that can stably store up to four electrons per molecule. By increasing the size of aromatic systems, the solubility of the materials is greatly reduced as the result of enhanced π-π stacking potential as well as their dicationic nature. Our studies have revealed that the donor-acceptor (D-A) design in **2** with an electron-donating bithiophene bridge helps to enhance intramolecular charge transfer that improves the electronic conductivity, and the final battery performance. Moreover, to further extend the conjugated system within a polymer backbone, we also developed a new dibrominated building block **3**, for the synthesis of a series of conjugated polymers **CP1** and **CP2**. The main chain of these conjugated polymers is expected to reduce the twisting between the thiophene units because of the reduced steric repulsion between bithiophene and the alkynyl linkers, leading to a fairly co-planar extended backbone allowing for an efficient electron-conduction pathway. At the same time, the redox activity will largely be localized on the spatially separated, “pendant” carbonylpyridinium groups. As

cathode materials for LIBs, the prepared polymers present remarkably improved cyclability and rate performance, because of their high electrochemical activity and effective suppression of dissolution. Impressively, **CP2** delivers not only the highest capacity but also the best cycling stability in this series, reaching up to 540 mAh g^{-1} after 240 cycles at 0.5 A g^{-1}, and as such even competing with the best inorganic cathode materials. This work highlights the considerable potential of bio-derived carbonylpyridinium redox-active units for sustainable energy storage applications and provides strategy for how they can be improved in LIBs.

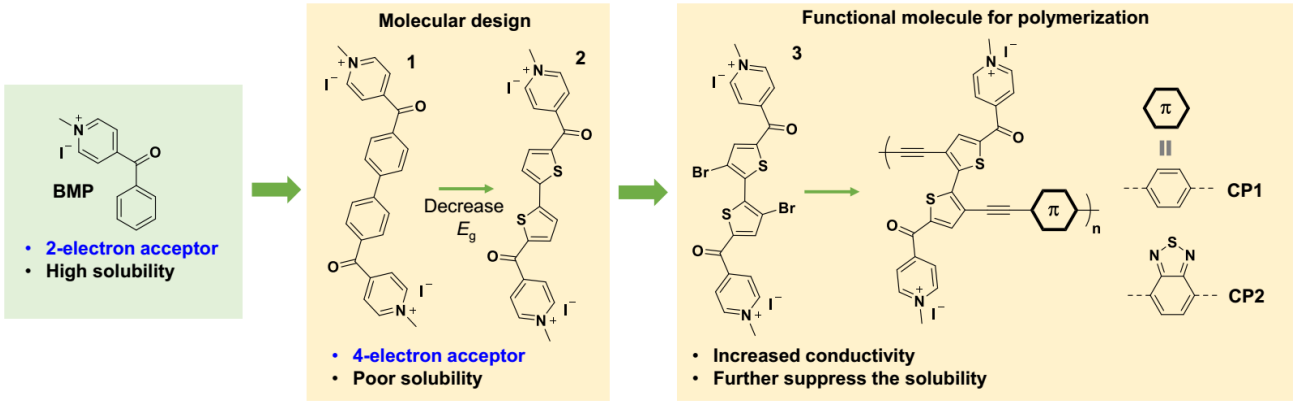

Scheme 1. Evolution of carbonylpyridinium based two-electron catholytes from small molecules to conjugated polymers.

RESULTS AND DISCUSSION

Synthesis and Characterization

Molecular compounds **1** and **2** can be easily synthesized in gram quantities from cheap commercially available starting materials in two steps with overall yields of 60-80 %. The synthetic route is presented in Figure 1a, and detailed procedures are provided in the Supporting Information. The key intermediates **S1** and **S2** were synthesized by regioselective lithiation of 4,4'-dibromobiphenyl or 5,5'-dibromo-2,2'-bithiophene with two equivalents of BuLi, followed by reaction of 4-cyanopyridine. This method gave the benzoylpyridine derivatives in high yields and good purity. Methylation of **S1** and **S2** by reaction with excess MeI in DMF at 90 ºC gave the desired carbonylpyridinium products (**1** and **2**) as pale-yellow solids with quantitate yields. Conveniently, due to the high reaction efficiency, no tedious column chromatography is needed to isolate the intermediates and final products in pure form. All the intermediates and final products were fully

characterized by ^{1}H and ^{13}C NMR spectroscopy, as well as high-resolution mass spectrometry (HRMS) (see SI). The structures of **1** and **S2** were further confirmed by single-crystal X-ray crystallography (Figure 1b and 1c). Common features are a highly planar central biphenylene or bithienylene bridge, while the carbonylpyridine (or pyridinium) units are twisted out of the central plane. The crystal data and structural refinement parameters are summarized in Table S1.

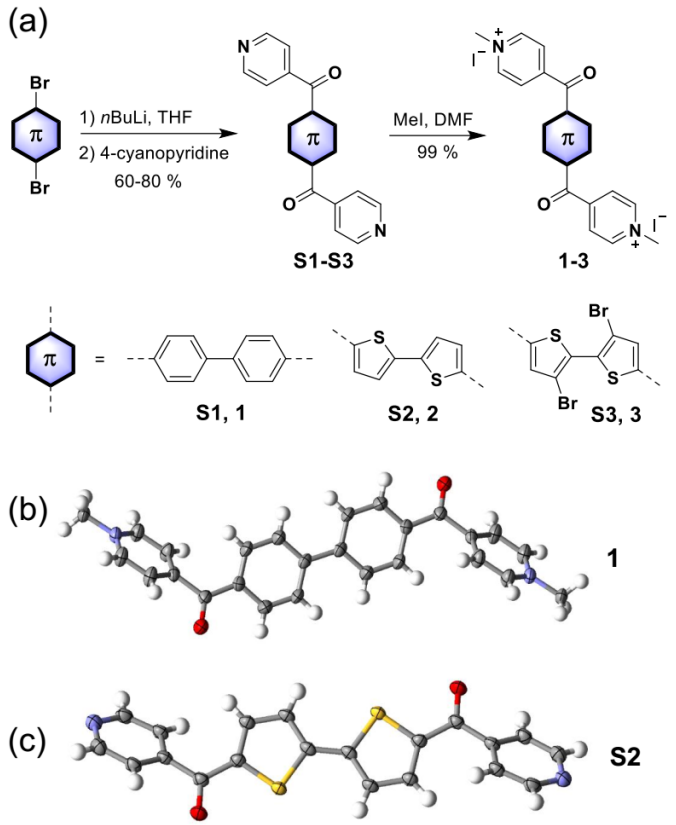

Figure 1. (a) Synthesis of **1-3**, (b, c) X-ray crystal structures of **1** and **S2**. The I^- anions of **1** are omitted for clarity.

To further extend the basic conjugated framework, a dibrominated compound **3** was designed that allows for subsequent cross-coupling reactions. The two-step synthesis of **3** is similar to that of **2**. Polymerization of **3** via Sonagashira coupling by reacting it with the corresponding arylethynylenes (4,7-diethynyl-2,1,3-benzothiadiazole or 1,4-diethynylbenzene) in the presence of $Pd(PPh_3)_2Cl_2$, CuI in DMF/Et_3N (1:1, v/v) afforded **CP1** and **CP2**, respectively. The resulting polymers are not soluble in either water, organic solvents, or organic carbonates (electrolyte), indirectly affirming their polymeric structure, and were thus easily purified by successively washing with excess DMF, methanol, dichloromethane, and finally diethyl ether.

The chemical structures of the polymers were verified by Fourier transform infrared (FTIR) spectroscopy and solid-state ^{13}C nuclear magnetic resonance (^{13}C NMR) spectroscopy. From the FTIR spectra (Figure S1), **CP1** and **CP2** exhibit strong peaks at $\bar{\upsilon}$ = 1640 and 1650 cm^{-1}, corresponding to the C=O stretching mode. Both polymers also display distinct a C≡C stretching vibration signal at 2180-2190 cm^{-1}, confirming the successful polymerization by connecting two monomers through a C≡C-bond. In addition, the 728 cm^{-1} band of **3** assigned to C-Br stretching, is absent in **CP1** and **CP2**, manifesting the completeness of the polymerization reaction. As observed from the ^{13}C NMR spectra (Figure S2), the signals at ca. 190 ppm support the existence of carbonyl carbon, while signals in the range of 120-150 ppm for **CP1** and **CP2** very likely arise from aromatic carbon atoms. The X-ray photoelectron spectra (XPS) of **CP2** confirmed the presence of C, O, S, N, and I atoms, as well as the absence of Br atoms, lending further support to the efficiency of the polymerization process (Figure S3 and S4).

Scanning electron microscopy (SEM) images show that **CP1** and **CP2** have a relatively uniform flower-like morphology (Figure 2a-d, S5), constructed from 2D nanosheets. The formation of this morphology can be explained by the synergistic polymerization and self-assembly process of the formed amphiphile polymers through hydrophobic-hydrophobic interaction and π–π stacking.[34] Such unique morphology is beneficial for exposing more redox-active sites and also minimized diffusion length for the transport of ions/electrons, thus potentially delivering a higher capacity and enhanced rate performance.[43] In contrast, undesirable fine-grained bulk morphologies were observed for **1** and **2**, probably resulting from tight molecular stacking, which is confirmed by their high crystalline nature. Powder X-ray diffraction (PXRD) patterns of **1** and **2** display several sharp reflection peaks at 2θ values of 5-30°. However, **CP1-CP2** are amorphous, as revealed by broad peak in the range of 20° to 25° in the PXRD pattern (Figure 2e). The Brunauer-Emmett-Teller (BET) surface areas for **CP1** and **CP2** were determined to be 24.1 and 41.3 m^2/g, respectively (Figure S6). Such small surface area was tentatively attributed to the strong stacking as a result of the largely linear and extended conjugated system. Thermogravimetric analysis (TGA, Figure S7) of the as-prepared polymers under N_2 unveils modest-to-high thermal stability. The decomposition temperatures (defined as the temperatures of 5% mass loss) were determined to be ca. 150 °C.

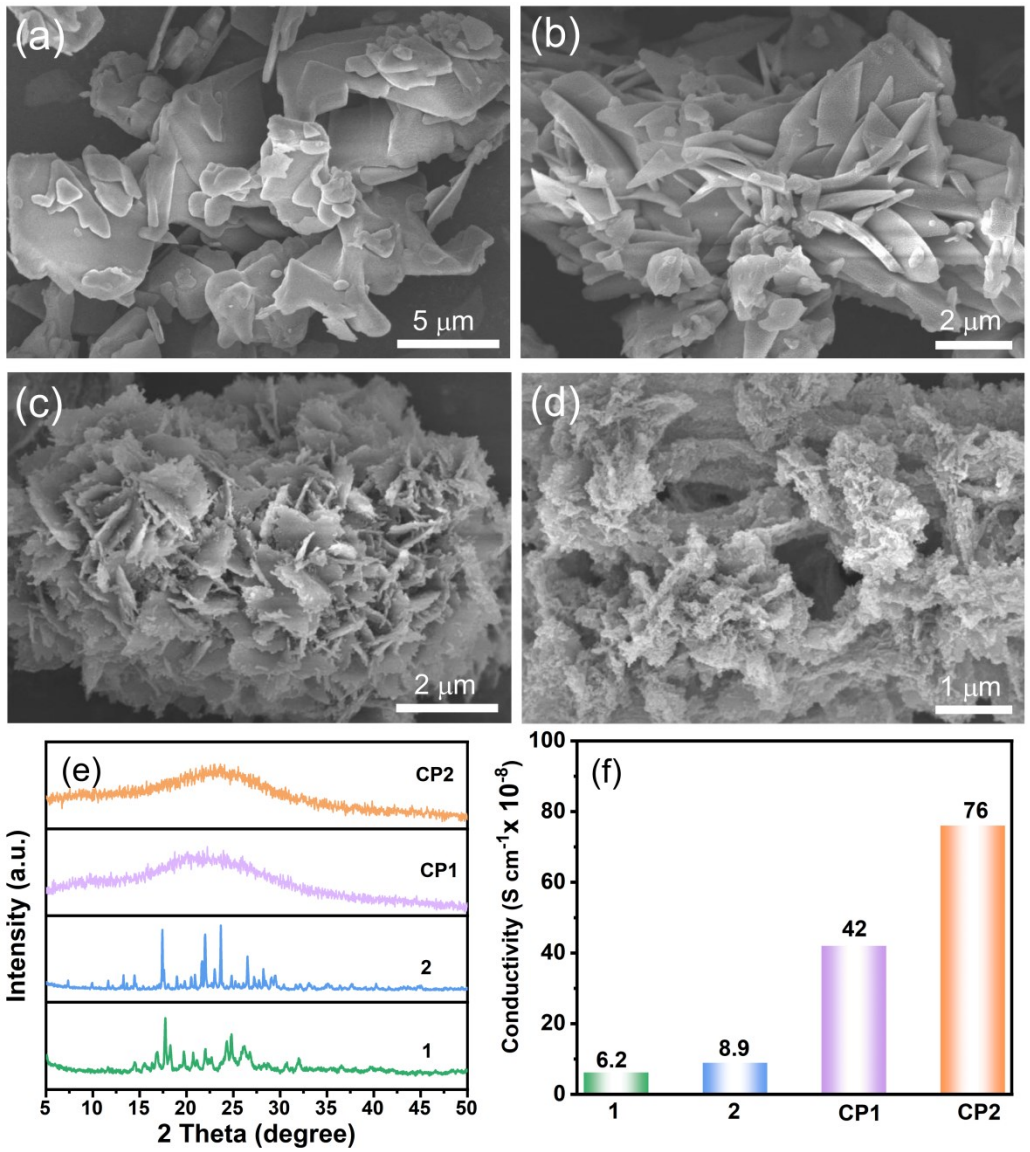

Figure 2. (a-d) SEM images of **1** (a), **2** (b), **CP1** (c) and **CP2** (d). (e) PXRD spectra and (f) electronic conductivities of **1**, **2**, **CP1**, and **CP2.**

The solubility and electrical conductivity of the electrode materials are fundamental factors in determining battery performance. Solubility measurements indicate that **1** and **2** are much less soluble in electrolyte (ethylene carbonate (EC), dimethyl carbonate (DMC) and ethyl methyl carbonate (EMC) (1:1:1, v/v)) than **BMP**. **BMP** has a high solubility exceeding 40 mg mL^{-1}, while those of **1** and **2** are 0.25 and 0.05 mg mL^{-1}, respectively. These results validate our design concept that the stronger intermolecular interaction (π–π stacking) can reduce the overall solubility, even for relatively small molecules. Polymerization further suppresses the solubility and two polymers (**CP1** and **CP2**) gratifyingly exhibit undetectable solubility. On

the other hand, as shown in Figure 2f, the conductivity measurement confirms that the electrical conductivity of **2** (8.9×10^{-8} S cm^{-1}) is slightly higher than that of **1** (6.2×10^{-8} S cm^{-1}), consistent with the D-A design that leads to relatively stronger intramolecular charge transfer. Notably, significantly improved electrical conductivity was observed for **CP1** (4.2×10^{-7} S cm^{-1}) and **CP2** (7.6×10^{-7} S cm^{-1}), up to an order of magnitude higher than those of the small molecules **1** and **2**.

Electrochemical and Optical Properties

The electrochemical properties of **1** and **2** were initially evaluated using cyclic voltammetry (CV). The CV measurements were conducted in DMF with 0.1 M tetrabutylammonium hexafluorophosphate ($TBAPF_6$) as a supporting electrolyte (Figure 3a). Compound **1** with biphenyl linker, demonstrates two well-separated two-electron transfer reduction waves at $E_{1/2}(1)$ = -1.05 V and $E_{1/2}(2)$ = -1.69 V (vs. Ag/Ag$^+$), and the profile is almost identical with that of **BMP**, except a slight positive shift (Figure S8). This suggests that the two redox-active carbonyl pyridinium units in **1** remain completely independent, which is in line with related systems.[44, 45] Compared with **1**, each pair of reduction waves in **2** is split into two, leading to the appearance of four reversible reduction waves, with the reduction potentials (vs. Ag/Ag$^+$) determined to be $E_{1/2}(1)$ = -0.97 V, $E_{1/2}(2)$ = -1.07 V, $E_{1/2}(3)$ = -1.60 V and $E_{1/2}(4)$ = -1.72 V. The reason could again be attributed to the intramolecular charge transfer due to the introduction of stronger electron-donating bithiophene linker. The peak-to-peak separation ($\Delta E_{p\text{-}p}$) for each wave is *ca.* 60 mV, indicating their good reversibility. In Figure 3b, the differential pulse voltammograms (DPV) further confirm the four-electron reduction processes of **1** and **2**, and the patterns are consistent with the CV. The CV of **3** is almost identical with that of **2** (Figure S9). In addition, a negligible loss of signal is observed in both cases after 10 continuous CV cycles at a scan rate of 100 mV/s, suggesting their excellent electrochemical stability. Overall, each carbonyl pyridinium unit can serve as two-electron storage unit. As such, compounds **1** and **2** can store up to four electrons per molecule. To make it more intuitive, the four-electron transfer processes are depicted in Figure 3c. The first two-electron reduction event leads to the formation of neutral radical species, and the second two-electron reduction produces the formation of anionic species, in line with the electrochemical data for BMP reported in the literature.[40, 42]

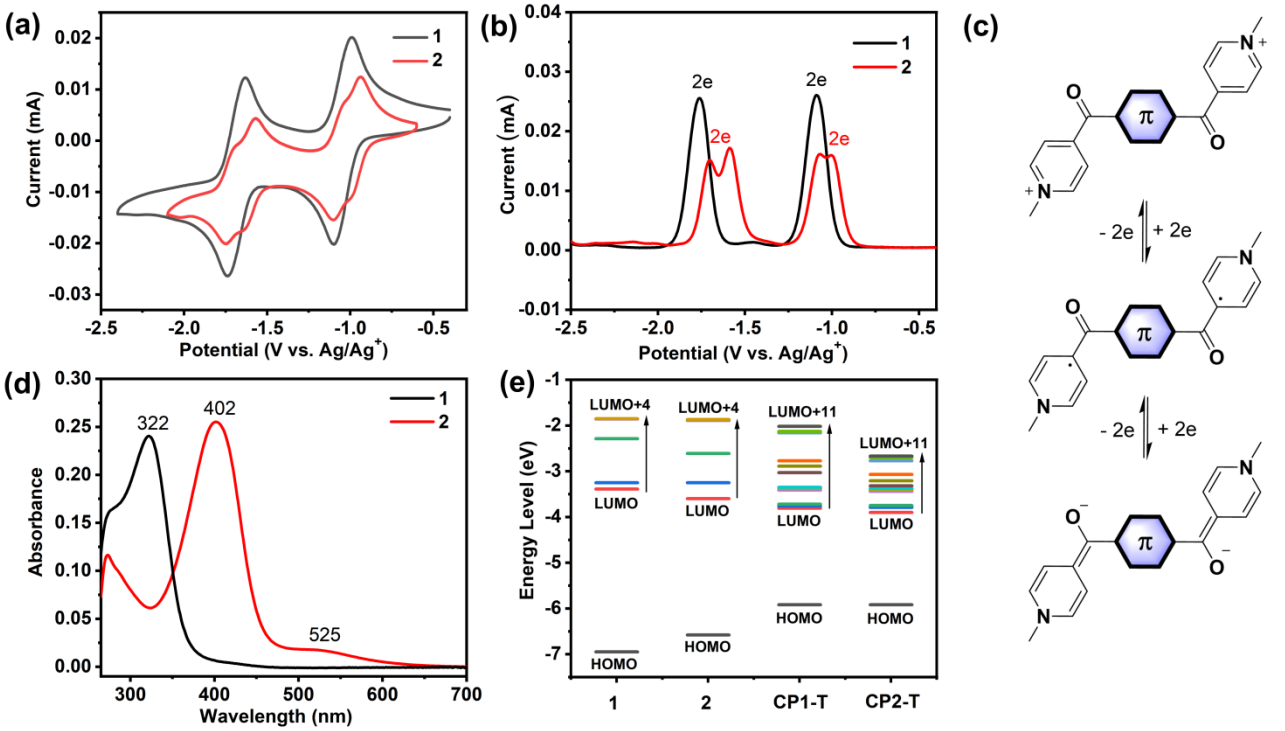

Figure 3. (a) Cyclic voltammogram (CV) of **1** and **2** in DMF solution (c = 1 mM) with 0.1 M $TBAPF_6$ as the electrolyte. (b) DPV of **1** and **2** in DMF solution (c = 1 mM) with 0.1 M $TBAPF_6$ as the electrolyte, parameters: increase E = 4 mV, amplitude = 50 mV, pulse width = 60.0 ms, sampling width = 20.0 ms, pulse period = 500.0 ms. (c) Reversible four reduction process for **1** and **2**. (d) UV-vis spectra of **1** and **2** in DMF solution. (e) The energy levels of HOMO and LUMOs of **1**, **2**, **CP1-T**, and **CP2-T** obtained by DFT calculations.

In dilute DMF solution, the π to π* absorption peak maximum of **2** is located at λ_{max}= 402 nm, which is 80 nm red-shifted compared to **1** at λ_{max} = 322 nm (Figure 3d). Moreover, **2** exhibits an additional low-energy absorption shoulder at 525 nm, which is attributed to intramolecular charge transfer from electron-donating bithiophene to carbonylpyridinium units. From the onset of the absorption (**1**: λ_{onset}= 375 nm; **2**: λ_{onset}= 600 nm), a narrower energy band gap (E_g = 2.07 eV) is determined for **2** compared to **1** (E_g = 3.31 eV). Based on the equation E_{LUMO} = -[E^{red}_{onset}-E(Fc/Fc$^+$) + 4.8] eV, the lowest unoccupied molecular orbital (LUMO) energies were calculated to be -3.8 eV for both **1** and **2**. While the same LUMO energy level means that both compounds have identical electron affinity, the narrow band gap for **2** indicates its high electron conductivity, which is confirmed by the conductivity measurement.

To obtain a better understanding of the photophysical and electronic properties, density functional theory (DFT) calculations for small molecules and polymers were performed at the B3LYP/6-31G(d) level of theory using the polarizable continuum model (PCM) solvation model (solvent: CH_3CN). The polymers were modeled as short chains containing three structural units (**CP1-T** and **CP2-T**) to keep the calculations manageable. The frontier orbitals diagrams, optimized structures and the coordinates are included in the SI (Figures S10-S14, Table S3-S6). For small molecules **1** and **2**, the highest occupied molecular orbitals (HOMOs) are localized over the biphenyl or bithiophene linker. The calculated energy gap between HOMO and LUMO for **1** is larger than **2**, consistent with the experimental trend. The contour plots of the five lowest unoccupied orbitals (LUMO to LUMO+4) reveal that LUMOs are largely distributed on the carbonylpyridinium units. Representative frontier orbitals HOMO, and LUMO to LUMO+4 as well as the calculated orbital energy levels are shown in Figure 3e. The energy gaps between LUMO and LUMO+1, LUMO+3 and LUMO+4 are very small (less than 0.35 eV, indicative of their degenerative nature). Interestingly, the LUMO+2 orbitals display a large contribution from the central linker, indicating that the extended linker may also play a role in accepting electrons. It is well-known that the LUMO energy level of n-type electroactive materials is a useful parameter for estimating its relative redox potential (a lower LUMO energy level corresponds to a higher reduction potential). Assuming that the electron configurations are rigid, electrons will successively fill the unoccupied orbitals from the lowest to the highest-energy orbital during the reduction process.

The optimized structures of **CP1-T** and **CP2-T** reveal high planarity of the extended conjugated backbone (main chain. Figures S11-S12), where majorly contribute to the HOMOs. Analogous to small molecules **1** and **2**, the LUMOs of the two polymers are also mostly located on the carbonylpyridinium units. Both polymers exhibit a dozen of low-lying orbitals from LUMO to LUMO+11 that could potentially be involved in relevant reductive processes (the lower/upper values are -3.8/-2.1 eV for **CP1-T**, -3.9/-2.7 for **CP2-T,** Figure 3e). Moreover, the introduction of an electron-withdrawing benzothiadiazole unit significantly lowers the LUMO in **CP1-T**.

Lithium-ion battery test

For the investigation of **1**, **2, CP1**, and **CP2** as active materials in LIBs, we fabricated composite electrodes containing 60 wt% of active material, 30 wt% carbon black (ECP-600JD) as the conductive additive, and 10 wt% polyvinylidene fluoride (PVDF) binder. A lithium metal disk was used as the counter electrode and $LiPF_6$ (1.0 M) in a mixture of ethylene carbonate (EC), dimethyl carbonate (DMC) and ethyl methyl carbonate (EMC) (1:1:1, v/v) with 1% vinylene carbonate (VC) was used as the electrolyte. The cells were first evaluated using cyclic voltammetry (CV) over the voltage range of 0.05-3.0 V vs Li/Li^+ at 0.2 mV s^{-1}. As shown in Figure 4a-b, the two polymers show two quasi-reversible anodic peaks at 1.35 and 2.20 V (vs Li/ Li^+), that are comparable to the performance of small molecules and related polymers in our previous report.[42] In addition, the peak-to-peak area under the electrochemical event at 2.20 V were enhanced for **CP2** as result of the introduction of benzothiadiazole unit as an additional redox center. This could consequently improve the capacity of the battery. In comparison, the two small molecules **1** and **2** exhibit less-obvious peaks (Figure S15), probably due to their undesired bulk morphologies, which hampers the effective full utilization of the redox-active units.

As an important parameter in LIBs that is greatly influenced by the solubility, the long-term cyclability was first investigated. Figure 4c presents the cycling performance with a high coulombic efficiency of **1**, **2**, **CP1** and **CP2** at a current density of 0.5 A g^{-1}. During the first 30 cycles, all electrodes showed a steady decay in capacity, and the capacity values in a certain cycle follow the trend of **1** < **CP1** < **2** < **CP2**. The capacity loss in the first few dozen cycles is mainly ascribed to the electrolyte decomposition and the formation of solid electrolyte interphase (SEI) film, which is often observed for organic battery electrodes.[46-50] The electrodes based on compounds **1**, **2**, **CP1** and **CP2** deliver reasonable capacities of 196, 293, 291 and 390 mAh g^{-1} after 30 cycles. (Figure 4c). In subsequent cycles, the capacity of **2** stabilized at 260 mAh g^{-1}, while **1** further underwent gradual capacity decay to 100 mAh g^{-1} after 240 cycles. The relatively poor cycling stability of **2** can easy be ascribed to its partial dissolution of in the electrolyte. However, its cycling stability is still much better than that of **BMP**, which exhibits a rapid capacity fading with only 50 mAh g^{-1} after 480 cycles (Figure S16). In comparison, the **CP1**- and **CP2**-based electrodes display a gradually increased capacity in the following cycles,

measured to be 360 mAh g^{-1} (**CP1**) and 540 mAh g^{-1} (**CP2**) after 240 cycles, respectively. This phenomenon can be attributed to electrode conditioning that provides more efficient conductive pathways as the electrode repeatedly swells and expels ions during charging and discharging cycles. Such behavior has also been observed in other lithium-organic hybrid batteries before. Notably, the capacity of **CP1** outperforms **2** after 45 cycles, and a new trend **1** < **2** < **CP1** < **CP2** occurs during cycles 45-240. These results suggest that conjugated polymers deliver the best cycling stability, resulting from high electrochemical activity and effective suppression of dissolution. We attribute the highest capacity observed for **CP2** to the introduction of benzothiadiazole unit as an additional redox center, which has already been demonstrated in our previous work.[27, 42] Moreover, their Coulombic efficiencies are close to 100% in all cases, verifying the high reversible redox stability of the carbonylpyridinium units. Overall, the varying dissolution behavior of the four materials agrees well with their different cycling performance, thus leading us to believe that unfavorable dissolution (and not chemical decomposition of the materials) is the dominating factor in capacity fading.

The rate performances were evaluated at various current densities from 0.2 to 5 A g^{-1} (Figure 4d). At a low current density of 0.2 A g^{-1}, electrodes based on **1**, **2**, **CP1**, and **CP2** exhibited stable discharge capacities of 350, 520, 360, and 520 mAh g^{-1}, respectively. The discharge capacities monotonically decrease with increasing current densities but more drastically in the case of two small molecules **1** and **2**. The detailed data are summarized in Table S2. This observation could be attributed to kinetic factors, such as lithium-ion diffusion and electron-transfer rates that limit the amount of charge extracted from the electrode at higher currents. Impressively, the two conjugated polymers again display superior rate performances than the small molecules. Relative to their specific capacity at 0.2 A g^{-1}, their capacity retentions at 1 and 5 A g^{-1} are 46 % and 22 % for **1**, 50 % and 22 % for 2, 64 % and 40 % for **CP1**, 70 % and 44 % for **CP2**, respectively. Although **CP1** displays lower capacity than **2** at low current densities (< 1 A g^{-1}), it catches up with increasing current, which is consistent with the observed cycling performance. The excellent rate performance of the conjugated polymers is not only the result from their absolute insolubility, but also their enhanced electronic conductivity. In addition, their amorphous morphology in the microscale range probably allows the full utilization of the redox-active sites and also minimizes diffusion length for the transport of ions/electrons, thus delivering a higher actual capacity and enhanced rate performance. Importantly, when the current density is shifted

back from 5 A g^{-1} to 0.2 A g^{-1}, nearly quantitative recovery of the initial capacities is observed in all the cases, demonstrating the superior stability.

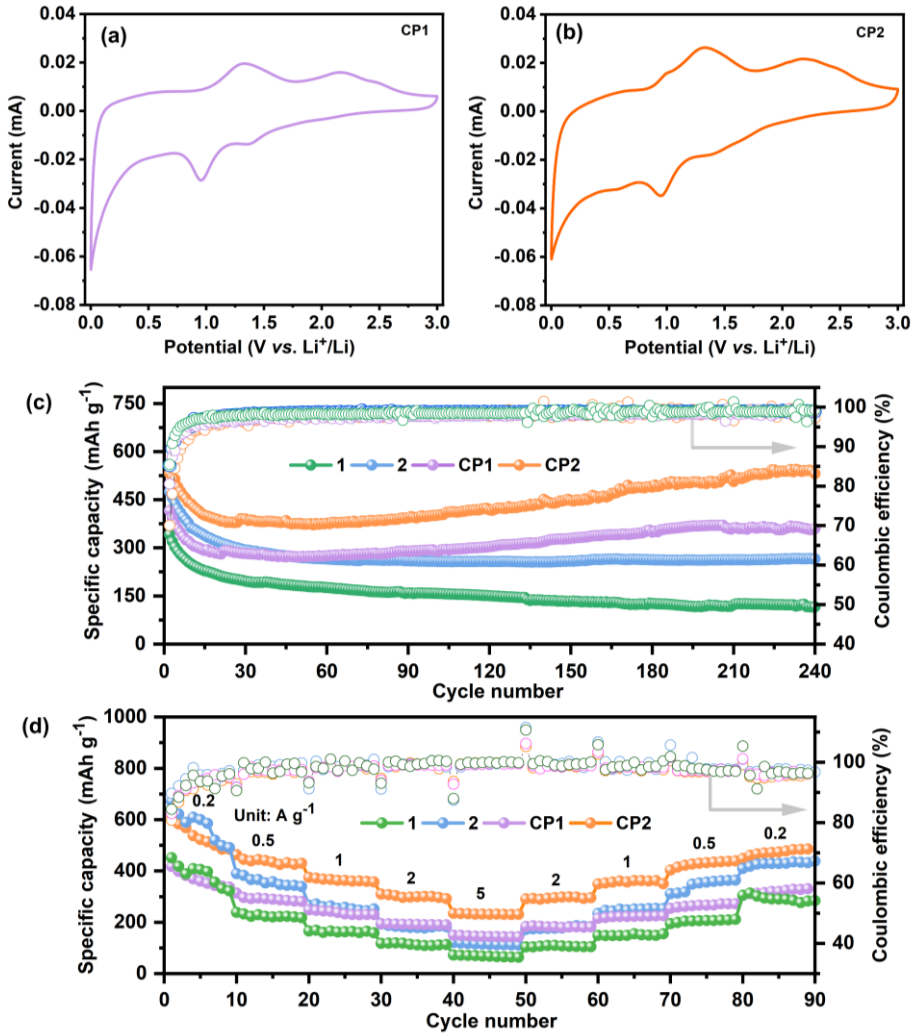

Figure 4. (a-b) CV curves of **CP1** and **CP2** electrodes in a battery configuration at 0.2 mV s^{-1}. (c) Cycling performance of **1**, **2**, **CP1**, and **CP2** at 0.5 A g^{-1}. (d) Rate performance of **1**, **2**, **CP1**, and **CP2** at different current densities.

Overall, the stepwise improvement of the rate performance and cycling stability on going from **1** via **2** to **CP1** and finally **CP2**, is consistent with their inherent electrical conductivity, solubility, and morphology. Impressively, **CP2** delivers not only the highest capacity but also the best cycling stability (Figure 4c-d), suggesting high electrochemical activity and effective suppression of dissolution. To our knowledge, the rate capability and cycling stability of **CP2** is one of the best reported for organic Li-ion batteries. Compared to many other well-known cathode materials for Li-ion batteries, such as inorganic $LiCoO_2$ (140 mAh g^{-1}), TEMPO (radical) functionalized polymethcarylate (PTMA, 111

mAh g^{-1}),[8] polyanthraquinone (263 mAh g^{-1})[14], poly(chalcogenoviologen)s (463 mAh g^{-1} at 0.5 A g^{-1}),[33] and other previously reported bio-derived polymeric cathode materials (< 150 mAh g^{-1}),[51-55] our polymer provides among the highest specific capacity, making this current system highly desirable as an organic cathode material for lithium-ion battery applications.

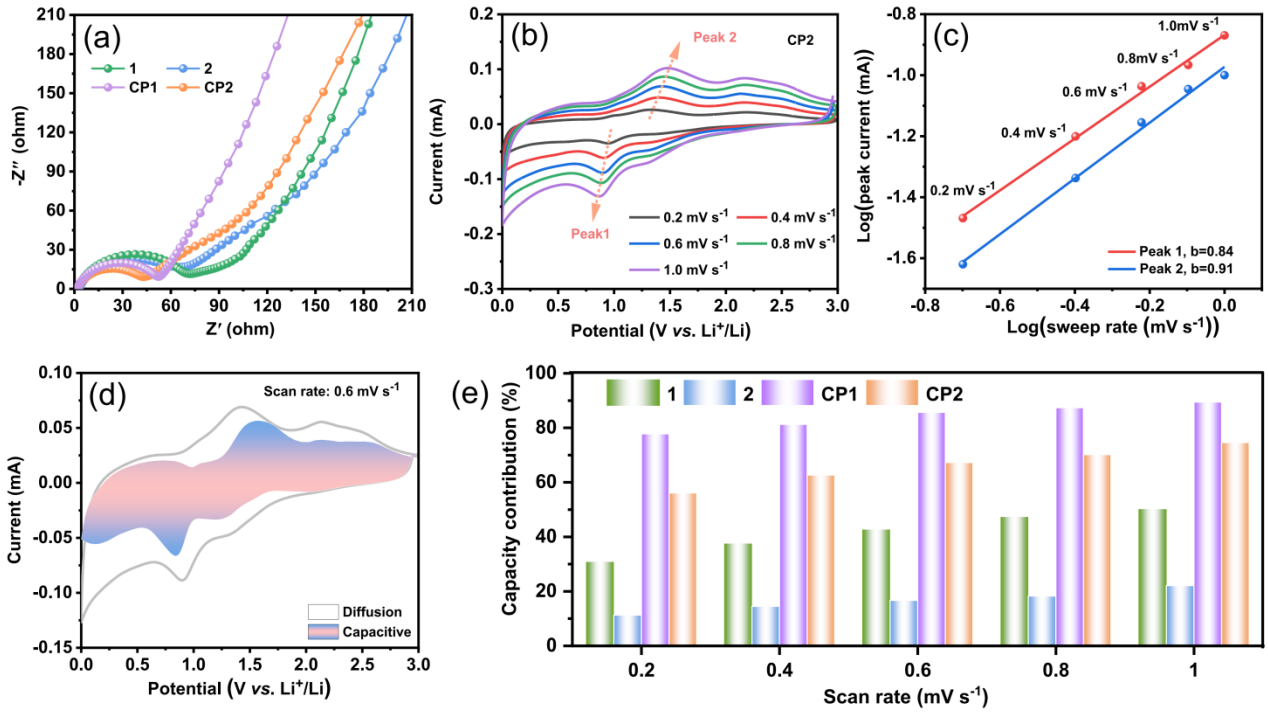

Figure 5. (a) EIS spectra of **1**, **2**, **CP1,** and **CP2** electrodes before cycling. (b) CV curves of **CP2** at different scan rates. (c) Log *i* versus log *v* plots of **CP2** to determine the *b* values of different peaks. (d) Capacitive contributions of **CP2** in CV curve at 0.6 mV s^{-1}. (e) Capacitive contributions (in percentage) of **1**, **2**, **CP1,** and **CP2** at different scan rates.

The electrochemical kinetics were investigated using electrochemical impedance spectroscopy (EIS; Figure 5a). The charge-transport resistances (R_{ct}, denoted by the diameter of the semicircle in high- and intermediate-frequency region) became smaller from **1** (70 Ω) < **2** (65 Ω) < **CP1** (52 Ω) < **CP2** (43 Ω), supporting an improved electrical conductivity by extending the conjugation and improving charge transfer. These values are consistent with the conductivity measurements (vide supra). Furthermore, to better understand the Li^+ diffusion process, the diffusion coefficients (D_{Li}^+) of the four electrodes were calculated from the Warburg region (see the SI for details). The D_{Li}^+ values of **1**, **2**, **CP1**, and **CP2** were calculated to be 6.64×10^{-14} cm^2 S^{-1}, 8.54×10^{-14} cm^2 S^{-1}, 1.42×10^{-13}, and 3.12×10^{-13}, respectively. The highest D_{Li}^+ value of **CP2** indicates faster lithium-ion diffusivity, consistent with the battery test data.

The reaction kinetics were further studied by conducting cyclic voltammetry on the four materials at various scan rates. As seen from the CV profiles of **CP2** at various sweep rates (0.2 to 1.0 mV s^{-1}; Figure 5b), multiple redox peaks were continuously observed at various scan rates. With elevated scan rates, the cathodic peaks shift to lower potentials, while the anodic peaks shift to higher potentials, which we ascribe to the enhanced polarization (Figure 5b and Figure S17-S20). In the linear fits of the natural logarithm (ln) of peak current vs. scan rate, the slopes for anodic and cathodic peaks for the two conjugated polymers (0.84-0.95) are higher than those of the two small molecules (0.65-0.85), indicating more capacitance contribution in reaction kinetics of polymers (Figure 5c and Figure S17-S20). More accurately, the capacity contribution to the total capacity can be evaluated by the equation: $i = k1v^{1/2} + k2v$, where $k1v^{1/2}$ and $k2v$ represent the diffusion-controlled and capacitive-controlled contributions, respectively. At a fixed potential of 0.2 mV s^{-1}, capacitive contributions were determined to be 30%, 11%, 78% and 56% for **1**, **2**, **CP1** and **CP2**, respectively. Increasing the scan rate led to higher capacitive contributions in all cases, and the values are summarized in Figure 5e. The higher capacitive contributions with the two conjugated polymers indicate fast insertion and extraction of Li-ions, which is favorable for fast charge storage and long-term cyclability. Overall, these results further confirm high rate and long cycling performance of the conjugated polymers, consistent with the battery test data.

The interaction of **CP1** and **CP2** with lithium-based entities was further analyzed by ex-situ FTIR and ex-situ XPS spectroscopies. As shown in Figure 6a, the intensity of C=O peak at 1650 cm^{-1} of the benzoyl-*N*-methylpyridinium unit of **CP2** gradually decreased during discharge (0.005 V vs. Li/Li^+), suggesting the reduction process and lithium insertion. The carbonyl peak was found to recover again upon charging, indicating complete reversibility of this reaction. The ex-situ XPS data further confirm that the cycled reduction/oxidation and lithium/de-lithiation process. In the C 1s spectra in Figure 6b, the characteristic peak assigned to the C=O bond at 288.6 eV disappears after discharged to 0.005 V, along with the emergence of new peak at 287.1 eV which was attributed to the reduced C-O bond. Subsequent recharging to 3.0 V led to the re-appearance of the C=O peak, suggesting its good reversibility. A C-Li peak (289.2 eV) was also observed during the discharge, which may result from the superlithiation process and/or the SEI formation. In the O 1s spectra in Figure 6c, the obvious signal of C=O at 530.5 eV is shifted to the C-O-Li at 531.4 eV in the initial discharge process and partially recovered at the fully charged state, suggesting the lithiation and de-lithiation process during

the reduction and oxidation reactions. These XPS data are consistent with the FTIR data, demonstrating the relatively good stability during the charging and discharging cycles. In addition, SEM analysis of the electrodes after 90 cycles revealed no obvious morphology changes compared to the fresh cells for both small molecules and polymers, further confirming their high electrochemical stability (Figure S21).

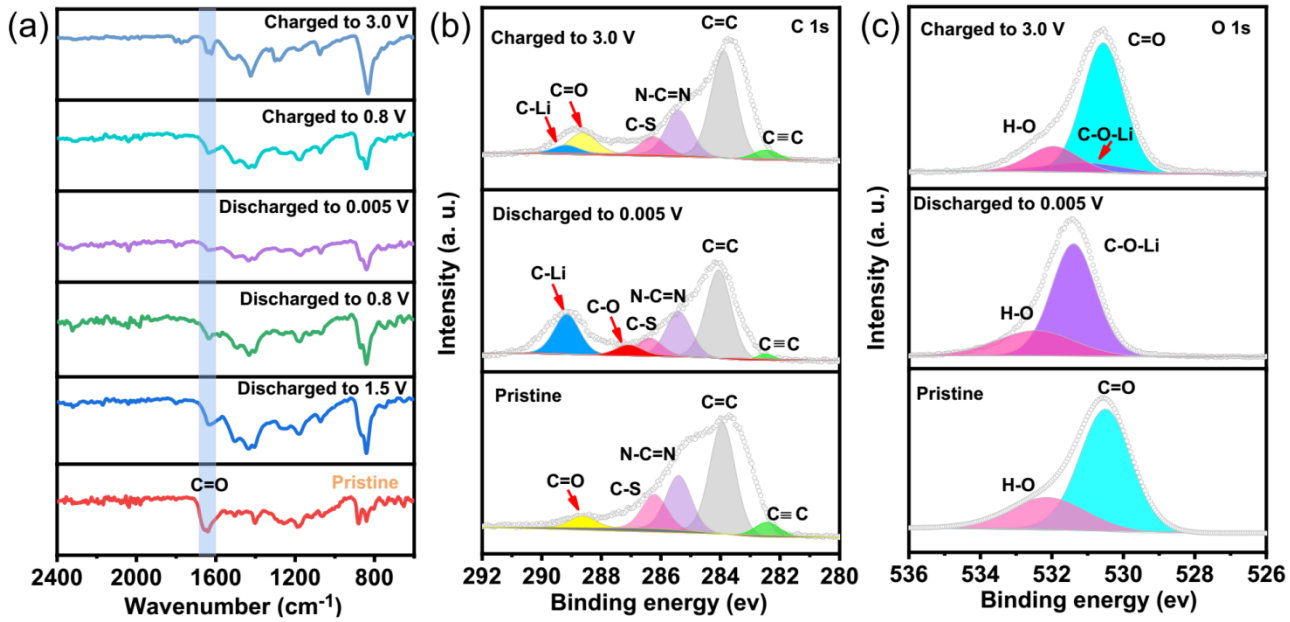

Figure 6. (a) Ex-situ FTIR and (b-c) C 1s and O 1s XPS spectra of the **CP2** electrode recorded at different charge states.

CONCLUSIONS

With the aim to improve the energy and high-power density of Li-organic hybrid batteries, the development of organic molecules with multiple redox centers, limited solubility and high conductivity is highly desirable. In the current work, we report a rational design strategy to suppress the dissolution and enhance the conductivity of such active materials from small molecules **1** and **2** to conjugated polymers **CP1** and **CP2** in stepwise fashion toward realizing high performance LIBs. Compounds **1** and **2** can reversibly store up to four electrons and show greatly decreased solubility compared to **BMP** as a result of strong intermolecular interactions. The donor-acceptor (D-A) character of **2** helps enhancing the intramolecular charge transfer, thereby improving the electronic conductivity and ultimately, battery performance. Both cycling stability and rate performance are further enhanced through the polymerization, as a result of high electrochemical activity and effective suppression of dissolution. Impressively, polymer **CP2** delivers not only the highest capacity, but also the best cycling

stability, reaching up to 540 mAh g^{-1} after 240 cycles at 0.5 A g^{-1}. We believe that this work provides a promising carbonylpyridinium-based building block featuring multiple redox centers, on the way to competitive high performance Li-organic batteries.

Acknowledgements

This work was supported by the National Natural Science Foundation of China (No.51703166 and No.22105121) and the Innovation Capability Support Program of Shaanxi (No.2020TD024). X. W. acknowledges the financial support from China Postdoctoral Science Foundation (No.2020M683419). X. H. thanks Shaanxi Normal University for the funding support. T. B. thanks the Canada Research Chairs program for support.

References

1. M. Li, J. Lu, Z. Chen and K. Amine, *Adv. Mater.*, 2018, **30**, 1800561.
2. M. Armand and J. M. Tarascon, *Nature*, 2008, **451**, 652-657.
3. Z. Song and H. Zhou, *Energy Environ. Sci.*, 2013, **6**, 2280-2301.
4. J. Kim, J. H. Kim and K. Ariga, *Joule*, 2017, **1**, 739-768.
5. T. B. Schon, B. T. McAllister, P.-F. Li and D. S. Seferos, *Chem. Soc. Rev.*, 2016, **45**, 6345-6404.
6. S. Lee, G. Kwon, K. Ku, K. Yoon, S.-K. Jung, H.-D. Lim and K. Kang, *Adv. Mater.*, 2018, **30**, 1704682.
7. Y. Lu and J. Chen, *Nat. Rev. Chem.*, 2020, **4**, 127-142.
8. K. Nakahara, S. Iwasa, M. Satoh, Y. Morioka, J. Iriyama, M. Suguro and E. Hasegawa, *Chem. Phys. Lett.*, 2002, **359**, 351-354.
9. K. Zhang, Y. Hu, L. Wang, J. Fan, M. J. Monteiro and Z. Jia, *Polym. Chem.*, 2017, **8**, 1815-1823.
10. K. Oyaizu, Y. Ando, H. Konishi and H. Nishide, *J. Am. Chem. Soc.*, 2008, **130**, 14459-14461.
11. C. Karlsson, T. Suga and H. Nishide, *ACS Appl. Mater. Interfaces*, 2017, **9**, 10692-10698.
12. D. L. Williams, J. J. Byrne and J. S. Driscoll, *J. Electrochem. Soc.*, 1969, **116**, 2.
13. Y. Lu, X. Hou, L. Miao, L. Li, R. Shi, L. Liu and J. Chen, *Angew. Chem. Int. Ed.*, 2019, **58**, 7020-7024.
14. Z. Song, Y. Qian, M. L. Gordin, D. Tang, T. Xu, M. Otani, H. Zhan, H. Zhou and D. Wang, *Angew. Chem. Int. Ed.*, 2015, **54**, 13947-13951.
15. W. Choi, D. Harada, K. Oyaizu and H. Nishide, *J. Am. Chem. Soc.*, 2011, **133**, 19839-19843.
16. X. Han, G. Qing, J. Sun and T. Sun, *Angew. Chem. Int. Ed.*, 2012, **51**, 5147-5151.
17. W. Huang, Z. Zhu, L. Wang, S. Wang, H. Li, Z. Tao, J. Shi, L. Guan and J. Chen, *Angew. Chem. Int. Ed.*, 2013, **52**, 9162-9166.
18. W. Luo, M. Allen, V. Raju and X. Ji, *Adv. Energy Mater.*, 2014, **4**, 1400554.
19. J. Yang, P. Xiong, Y. Shi, P. Sun, Z. Wang, Z. Chen and Y. Xu, *Adv. Funct. Mater.*, 2020, **30**, 1909597.
20. T. Matsunaga, T. Kubota, T. Sugimoto and M. Satoh, *Chem. Lett.*, 2011, **40**, 750-752.
21. Z. Lei, Q. Yang, Y. Xu, S. Guo, W. Sun, H. Liu, L.-P. Lv, Y. Zhang and Y. Wang, *Nat. Commun.*, 2018, **9**, 576.
22. M. Kolek, F. Otteny, P. Schmidt, C. Mück-Lichtenfeld, C. Einholz, J. Becking, E. Schleicher, M. Winter, P. Bieker and B. Esser, *Energy Environ. Sci.*, 2017, **10**, 2334-2341.
23. F. Otteny, G. Studer, M. Kolek, P. Bieker, M. Winter and B. Esser, *ChemSusChem*, 2020, **13**, 2232-2238.
24. P. Acker, L. Rzesny, C. F. N. Marchiori, C. M. Araujo and B. Esser, *Adv. Funct. Mater.*, 2019, **29**, 1906436.
25. J. A. Kowalski, M. D. Casselman, A. P. Kaur, J. D. Milshtein, C. F. Elliott, S. Modekrutti, N. H. Attanayake, N. Zhang, S. R. Parkin, C. Risko, F. R. Brushett and S. A. Odom, *J. Mater. Chem. A*, 2017, **5**, 24371-24379.
26. K. Lee, I. E. Serdiuk, G. Kwon, D. J. Min, K. Kang, S. Y. Park and J. E. Kwon, *Energy Environ. Sci.*, 2020, **13**, 4142-4156.
27. L. Chen, C. R. Bridges, G. Gao, T. Baumgartner and X. He, *ACS Appl. Energy Mater.*, 2019, **2**, 7315-7320.
28. K. Oka, R. Kato, K. Oyaizu and H. Nishide, *Adv. Funct. Mater.*, 2018, **28**, 1805858.
29. C. Luo, O. Borodin, X. Ji, S. Hou, K. J. Gaskell, X. Fan, J. Chen, T. Deng, R. Wang, J. Jiang and C. Wang, *Proc. Natl. Acad. Sci. USA*, 2018, **115**, 2004-2009.
30. C. Luo, X. Ji, S. Hou, N. Eidson, X. Fan, Y. Liang, T. Deng, J. Jiang and C. Wang, *Adv. Mater.*, 2018, **30**, 1706498.
31. L. Striepe and T. Baumgartner, *Chem. Eur. J.*, 2017, **23**, 16924-16940.

32. M. Stolar, C. Reus and T. Baumgartner, *Adv. Energy Mater.*, 2016, **6**, 1600944.
33. G. Li, B. Zhang, J. Wang, H. Zhao, W. Ma, L. Xu, W. Zhang, K. Zhou, Y. Du and G. He, *Angew. Chem. Int. Ed.*, 2019, **58**, 8468-8473.
34. L. Chen, X. Zhu, Y. Zhang, G. Gao, W. Xue, S. Zhang, X. Wang, Q. Zhang and X. He, *J. Mater. Chem. A*, 2021, **9**, 18506-18514.
35. T. Ma, L. Liu, J. Wang, Y. Lu and J. Chen, *Angew. Chem. Int. Ed.*, 2020, **59**, 11533-11539.
36. J. Luo, B. Hu, C. Debruler and T. L. Liu, *Angew. Chem. Int. Ed.*, 2018, **57**, 231-235.
37. A. Jouhara, E. Quarez, F. Dolhem, M. Armand, N. Dupré and P. Poizot, *Angew. Chem. Int. Ed.*, 2019, **58**, 15680-15684.
38. N. Leventis, A.-M. M. Rawaswdeh, G. Zhang, I. A. Elder and C. Sotiriou-Leventis, *J. Org. Chem.*, 2002, **67**, 7501-7510.
39. N. Leventis, I. A. Elder, X. Gao, E. W. Bohannan, C. Sotiriou-Leventis, A. M. M. Rawashdeh, T. J. Overschmidt and K. R. Gaston, *J. Phys. Chem. B*, 2001, **105**, 3663-3674.
40. C. S. Sevov, D. P. Hickey, M. E. Cook, S. G. Robinson, S. Barnett, S. D. Minteer, M. S. Sigman and M. S. Sanford, *J Am. Chem. Soc.*, 2017, **139**, 2924-2927.
41. C. S. Sevov, K. H. Hendriks and M. S. Sanford, *J. Phys. Chem. C*, 2017, **121**, 24376-24380.
42. G. Gao, X. Wang, L. Chen, T. Baumgartner and X. He, *Chem. Mater.*, 2021, **33**, 4596-4605.
43. M. Wu, Y. Zhao, R. Zhao, J. Zhu, J. Liu, Y. Zhang, C. Li, Y. Ma, H. Zhang and Y. Chen, *Adv. Funct. Mater.*, 2021, **n/a**, 2107703.
44. M. Pan, Y. Lu, S. Lu, B. Yu, J. Wei, Y. Liu and Z. Jin, *ACS Appl. Mater. Interfaces*, 2021, **13**, 44174-44183.
45. P. Demay-Drouhard and T. Baumgartner, *J. Org. Chem.*, 2020, **85**, 14627-14633.
46. H. Kang, H. Liu, C. Li, L. Sun, C. Zhang, H. Gao, J. Yin, B. Yang, Y. You, K.-C. Jiang, H. Long and S. Xin, *ACS Appl. Mater. Interfaces*, 2018, **10**, 37023-37030.
47. T. Sun, Z.-j. Li, H.-g. Wang, D. Bao, F.-l. Meng and X.-b. Zhang, *Angew. Chem. Int. Ed.*, 2016, **55**, 10662-10666.
48. Z. Lei, X. Chen, W. Sun, Y. Zhang and Y. Wang, *Adv. Energy Mater.*, 2019, **9**, 1801010.
49. S.-B. Ren, W. Ma, C. Zhang, L. Chen, K. Wang, R.-R. Li, M. Shen, D.-M. Han, Y. Chen and J.-X. Jiang, *ChemSusChem*, 2020, **13**, 2295-2302.
50. X. Fan, F. Wang, X. Ji, R. Wang, T. Gao, S. Hou, J. Chen, T. Deng, X. Li, L. Chen, C. Luo, L. Wang and C. Wang, *Angew. Chem. Int. Ed.*, 2018, **57**, 7146-7150.
51. S. Admassie, T. Y. Nilsson and O. Inganäs, *Phys. Chem. Chem. Phys.*, 2014, **16**, 24681-24684.
52. Y. J. Kim, W. Wu, S.-E. Chun, J. F. Whitacre and C. J. Bettinger, *Adv. Mater.*, 2014, **26**, 6572-6579.
53. G. Milczarek and O. Inganäs, *Science*, 2012, **335**, 1468-1471.
54. T. B. Schon, A. J. Tilley, C. R. Bridges, M. B. Miltenburg and D. S. Seferos, *Adv. Funct. Mater.*, 2016, **26**, 6896-6903.
55. T. Y. Nilsson, M. Wagner and O. Inganäs, *ChemSusChem*, 2015, **8**, 4081-4085.

TOC

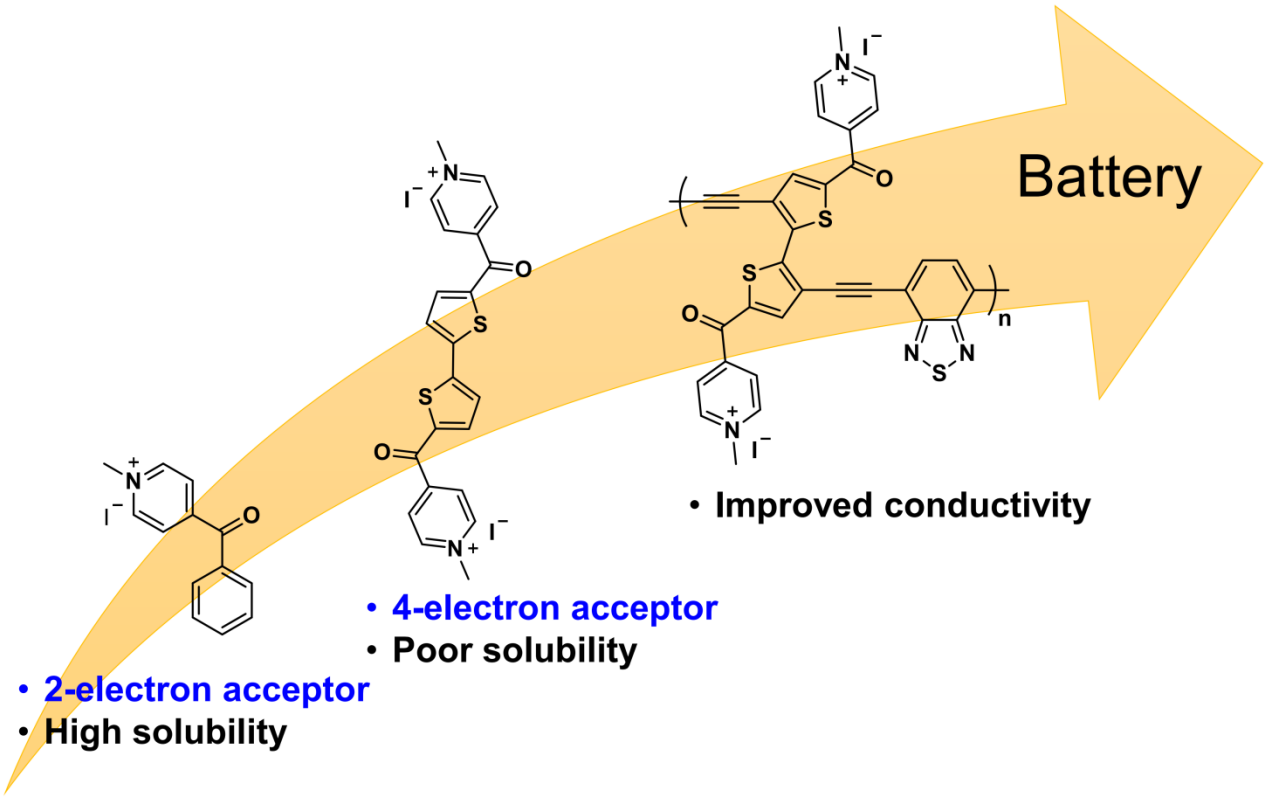
Battery
• 2-electron acceptor
• High solubility
• 4-electron acceptor
• Poor solubility
• Improved conductivity